Superalloys 2020 manuscript No.
(will be inserted by the editor)

3D Characterization of the Columnar-to-Equiaxed Transition in Additively Manufactured Inconel 718

Andrew T. Polonsky* · Narendran Raghavan · McLean P. Echlin · Michael M. Kirka · Ryan R. Dehoff · Tresa M. Pollock

Received: date / Accepted: date

Abstract Additive manufacturing (AM) provides enormous processing flexibility, enabling novel part geometries and optimized designs. Access to a local heat source further permits the potential for local microstructure control on the scale of individual melt pools, which can enable local control of part properties. In order to design tailored processing strategies for target microstructures, models predicting the columnar-to-equiaxed transition must be extended to the high solidification velocities and complex thermal histories present in AM. Here we combine 3D characterization with advanced modelling techniques to develop a more complete understanding of the solidification process and evolution of microstructure during electron beam melting (EBM) of Inconel 718. Full calibration of existing microstructure prediction models demonstrates the differences between AM processes and more conventional welding techniques, underlying the need for accurate determination of key parameters that can only be measured directly in 3D. The ability to combine multi-sensor data in a consistent 3D framework via data fusion algorithms is essential to fully leverage these advanced characterization approaches. Thermal modeling provides insight on microstructure development within isolated solidification events and demonstrates the role of Marangoni effects on controlling solidification behavior.

Andrew T. Polonsky
Materials Department, University of California Santa Barbara, Santa Barbara, CA 93106, USA
E-mail: polonsky@ucsb.edu
**Corresponding Author*

Narendran Raghavan
Computational Sciences and Engineering Division, Oak Ridge National Laboratory, Oak Ridge, TN 37830, USA
E-mail: raghavann@ornl.gov

McLean P. Echlin
Materials Department, University of California Santa Barbara, Santa Barbara, CA 93106, USA
E-mail: mechlin@ucsb.edu

Michael M. Kirka
Materials Science and Technology Division, Oak Ridge National Laboratory, Oak Ridge, TN 37830, USA
E-mail: kirkamm@ornl.gov

Ryan R. Dehoff
Materials Science and Technology Division, Oak Ridge National Laboratory, Oak Ridge, TN 37830, USA
E-mail: dehoffrr@ornl.gov

Tresa M. Pollock
Materials Department, University of California Santa Barbara, Santa Barbara, CA 93106, USA
E-mail: tresap@ucsb.edu

Keywords Additive manufacturing · Tomography · Solidification · Microstructure

1 Introduction

Since the advent of additive manufacturing (AM) in the 1980s, the process has been used for the development and design of rapid prototypes to inform ultimate geometries of traditionally-manufactured components. Additive manufacturing is no longer a rapid prototyping tool and is now being used to develop end products, with applications ranging from printed dental implants and rib cages to the manufacture of novel aerospace components. The interplay between processing conditions and ultimate performance of additive parts remains an area of intense study.

The scan strategy, or the manner in which the heat source traverses the bed, used during processing strongly influences the texture and microstructure of additive parts [1–3]. Differences in the default scan strategies employed by different machine manufacturers can further lead to parts printed from the same design having grossly different mechanical properties. The default scan strategies available to most users typically result in little control over the microstructure of a part, and commonly result in texture artifacts from changing scan patterns layer-to-layer [4]. Simple raster scan strategies can result in heavily textured samples with a highly columnar microstructure [5–9], which can be modified via beam scanning strategies designed to control the thermal gradient and initiate the columnar-to-equiaxed transition (CET) [10–13].

Due to the strong influence of microstructure on part properties, local microstructure control can similarly enable local control of part properties, such as gradient properties across a component, or improved mechanical properties around critical failure sites that arise from complex geometries. Printing AM parts with such target microstructures requires *a priori* knowledge of processing-microstructure relationships. Models of additive processes that focus on individual melt pools or single weld lines have shown the need to include temperature-dependent physics to capture the dynamics of the melt pool [14–16]. These models are often extensions of validated casting or welding models, and may not incorporate the complex fluid flow and thermal histories present in AM parts. A major limitation of these models is the extensive computation time; modeling a single track in a laser powder bed fusion (L-PBF) process can require tens to hundreds of thousands of processing hours [17], severely limiting the extension of these models to full-scale parts. Moreover, thermal models generally cannot directly predict microstructures from process parameters alone.

The change in thermal gradient and solid-liquid interface velocity during a solidification event can be calculated in high resolution using supercomputers [18], but to predict microstructure, thermal models must rely on separate descriptions of the CET, namely those developed by Hunt [19] and Gäumann [20]. These models provide a good basis for qualitative prediction of solidified microstructures, but incorporate the use of difficult to measure properties including solidification nuclei density, as well as alloy- and interface velocity-specific parameters. Additional ex situ characterization of additively manufactured parts on the length scale of the melt pool is required to validate and improve these models. The complex grain shapes, interplay of melt pool boundaries, and strong anisotropy developed in additive components makes 2D data and stereological approaches ineffective at fully assessing the microstructure.

In this work, the microstructure of an isolated melt pool in Inconel 718 was characterized in 3D, providing critical microstructural information needed for process models currently under development. The calibrated

process model was then used to investigate the influence of fluid flow and trace element impurities commonly found in AM powders on resultant microstructures.

2 Methodology

2.1 Experimental Characterization

2.1.1 Sample Fabrication

Bulk Inconel 718 was fabricated using gas atomized Inconel 718 powder feedstock with a particle size range of 40-120 µm from Praxair, Inc. in an Arcam S12 EBM. The build consisted of a block with dimensions of 20×20×15 mm ($l \times w \times h$). A nominal build layer thickness of 50 µm was used with a preheat temperature of 1000 °C. The block was fabricated using a bidirectional raster scan strategy. The electron beam traversed the part with a beam current of 20 mA at a speed of 4 m/s, with 0.10 mm spacing between adjacent lines. The beam was rotated by 18 ° between build layers. On the last layer of the build, powder was raked across the build surface before several isolated melt pools were created across the block surface. These spots were melted using an electron beam current of 10 mA with a dwell time of 0.5 ms. Samples of the bulk material from the build were analyzed for chemical composition. Major elements were characterized via inductively coupled plasma optical emission spectroscopy (ICP-OES). Trace elements were analyzed via either glow discharge mass spectroscopy (GDMS) or LECO combubstion analysis. Results of the chemical analyses are shown in Table 1. The sample material composition conforms to AMS specification 5662 for wrought Inconel 718 [21].

2.1.2 3D Data Acquisition

A sample of material containing an isolated melt pool as well as surrounding bulk material was removed from the top surface of the block via wire electrical discharge machining. 3D data was collected via TriBeam tomography [22–24], a serial-sectioning technique utilizing a femtosecond laser for large-scale material removal inside a scanning electron microscope (SEM). Electron Backscatter Diffraction (EBSD) data was collected in conjunction with secondary electron (SE) and backscatter electron (BSE) images from a volume roughly 1150×800×500 µm in size. EBSD data was collected with a 1.5 µm step size in a square grid with a sectioning slice thicknesses of 1.3 µm. A total of 897 slices of EBSD data were collected with an acquisition time of 20 minutes per slice, yielding 4.02 TB of raw data. BSE images were collected once every eight slices and used as a set of reference images for distortion correction and identification of the melt pool boundary.

2.1.3 Multimodal Data Fusion via the Thin Plate Spline

In order to leverage microstructural information present in various imaging modalities, a framework is required to fuse disparate imaging techniques into a coherent volume. Figure 1 shows data from an EBSD scan and BSE image taken from a region in the middle of the characterized volume. The melt pool boundary is clearly visible in the BSE image, but is not distinguishable in the EBSD scan data. In order to locate

Table 1 Chemical composition of the Inconel 718 Block and typical composition of wrought Inconel 718 given in weight percent.

Element	Measured	Conventional*
Nickel	54.4†	50-55
Chromium	17.5†	17-22
Iron	18.4†	balance
Niobium	4.80†	4.75-5.5
Molybdenum	3.08†	2.8-3.3
Titanium	0.878†	0.65-1.15
Aluminum	0.428†	0.2-0.8
Cobalt	0.108‡	≤1
Carbon	0.0321§	≤0.08
Manganese	0.0545‡	≤0.35
Silicon	0.246‡	≤0.35
Phosphorus	0.0080‡	≤0.015
Boron	0.0013‡	≤0.006
Nitrogen	0.0171§	—
Sulfur	0.0018§	≤0.015
Oxygen	0.0140§	—

* AMS 5662 specification [21]
† ICP-OES measurement
‡ GDMS measurement
§ LECO measurement

the melt pool boundary in the EBSD data, these two imaging modalities must be registered into a single reference frame.

This process can be complicated by the source of the signal used to generate an image; secondary electrons and backscattered electrons, for example, originate from different subsurface interaction volumes in the material. More important are geometric considerations within the vacuum chamber. At the high tilt angles used for EBSD collection, minor sample misalignment can create large apparent distortions. The use of image registration approaches such as scale-invariant feature transformation (SIFT), Harris corner detection, and mutual information have been used previously to correct such distortions, and more recently machine learning techniques have also been employed [25–29]. Here we take the approach for EBSD distortion correction described by Zhang et al. that employs the thin plate spline (TPS) for transformation [30] due to its ease of implementation and straightforward physical interpretation.

TPS is a 2D formulation of the cubic spline [31]; just as a 1D cubic spline can be understood as the bending of a beam along a set of fixed control points, so too can the thin plate spline be interpreted as the local bending of a thin plate with fixed control points along the plane. Control points act as anchors with smooth interpolation between the points, wherein the extent of local bending is determined by the local density of control points. The TPS algorithm is well suited for image registration between different reference frames, even if one frame is significantly distorted in relation to the other. The classic 2D formulation for the relation of two reference frames given n control points has been extended here to 3D and is given by Equation 1:

$$(X, Y, Z) = f(x, y, z) = a_1 + a_x x + a_y y + a_z z + \sum_{i=1}^{n} w_i U(|P_i - (x, y, z)|) \tag{1}$$

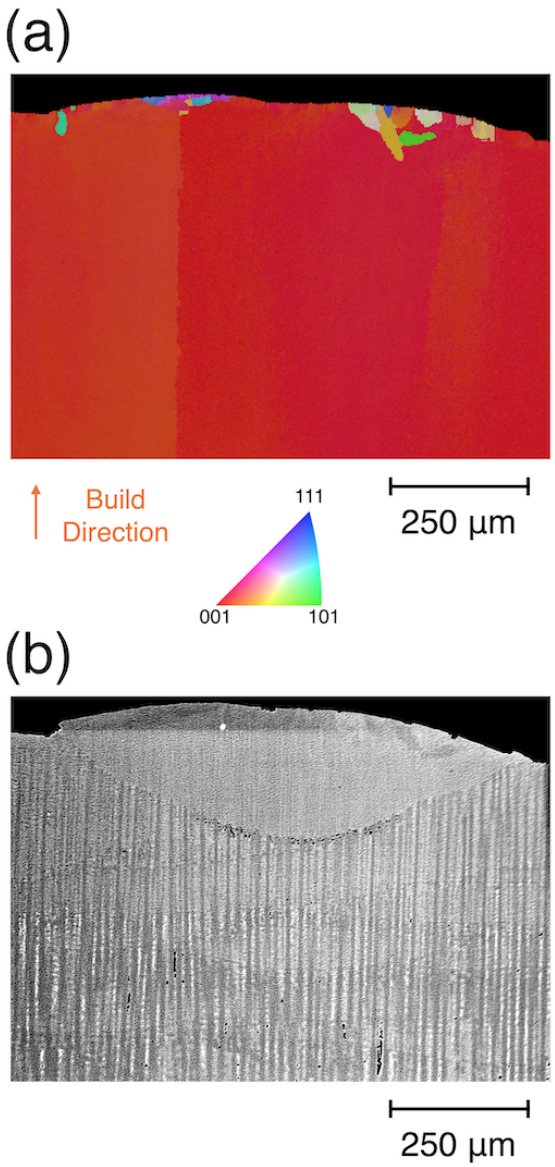

Fig. 1 EBSD map (a) and BSE image (b) from a single region of the characterized volume. The EBSD map reveals the presence of small grains that can not be identified in the BSE image, while the BSE image displays contrast along the melt pool boundary. No such contrast along the melt pool boundary can be identified in the EBSD map, where the base orientation of the substrate is maintained along the pool boundary.

where (X, Y, Z) is a point in the distorted frame, (x, y, z) is a point in the reference frame, $a_1 + a_x x + a_y y + a_z z$ represents the global affine transformation between the reference frames, and $\sum_{i=1}^{n} w_i U(|P_i - (x, y, z)|)$ represents the local non-affine (*bending*) portion of the transformation. U is the radial basis function given by Equation 2:

$$U(r) = r^2 log(r^2) \tag{2}$$

where r is the Euclidean distance between control point P_i and another point (x, y, z) in the same frame. Given the extra constraint of $U(0) = 0$, this radial basis function is a biharmonic solution to the equation for a thin plate lifted above the (x, y) plane, and therefore minimizes the overall bending of the plate [30,31].

The application of TPS in relating two reference frames requires knowledge of the values a_1, a_x, a_y, and a_z for the global affine transformation, and the weighting coefficients w_x, w_y, and w_z for each of the n control points for the bending portion of the transformation. Given these coefficients, the location of any point (X, Y, Z) in the distorted frame can be directly mapped to its corresponding location (x, y, z) in the reference frame.

These coefficients can be solved using a set of control points identified as corresponding locations within both the distorted and reference frames. For the 2D area shown in Figure 1, comprising roughly $200,000$ EBSD points, only 20 to 30 control points are needed to establish a good relation of reference frames. Typical choices for control points are features that can be distinguished in both BSE images and EBSD maps such as pores, precipitates, and grain boundary triple points. Calculation of the relevant transformation parameters is achieved by solving a set of linear equations, the details of which can be found elsewhere [30,31]. A total of 3894 control points were used to register the BSE and EBSD data together. The improved registration of the EBSD data was confirmed to match with optical profilometry data collected on the sample prior to 3D characterization.

2.1.4 Reconstruction of a Coherent Volume

Using TPS as detailed in Section 2.1.3, all relevant data arrays from each voxel of EBSD data were copied into the BSE reference frame. Reconstruction of the dataset was performed using the open-source DREAM.3D package [32]. Data was first masked using a minimum image quality (IQ) cutoff of 2.6 standard deviations less than the average measured value, providing good grain boundary contrast and following similarly to prior studies of IQ as a mask [33]. Data below this cutoff was included in the mask if at least four of its six nearest neighbors were within 2° of misorientation. Grains were segmented using a 2° misorientation tolerance amongst nearest neighbors, which has been shown to be a good segmentation tolerance for AM materials characterized in 3D [34]. Grains containing less than 8^3 voxels or having fewer than three nearest neighbors were considered too small to be accurately characterized and were removed, with the remaining space filled via an iterative coarsening of neighboring grains.

2.2 Solidification Modeling

The AM processing conditions used to print the melt pool sample were simulated in TRUCHAS, where 3D calculations of thermal gradients and solid-liquid interface velocities are achievable at micron length scales with sub-millisecond time scales that are otherwise inaccessible to modern in situ monitoring techniques [35]. TRUCHAS uses a mimetic finite difference discretization technique to solve the heat equation and additionally uses a finite volume discretization scheme to solve the momentum equation to incorporate fluid flow. A volumetric heat source function is defined to depict the heat source, and a radiation boundary condition is applied to the top surface. The details of the partial differential equations, boundary conditions, heat source model, and material properties of Inconel 718 used in the calculations can be found elsewhere [18]. Simulations both with and without fluid flow were conducted to study the effect of surface-active elements such as sulfur and oxygen, which are known to affect the temperature dependence of surface tension in Inconel 718 welds [36]. In temperature regimes where surface tension decreases with increasing temperature, radially outward fluid flows can develop in melt pools due to the imposed temperature gradient across the

melt pool (mass flux from regions of lower surface tension to regions of higher surface tension). Conversely, in temperature regimes where surface tension increases with increasing temperature, radially inward fluid flows can develop across the temperature gradient within a melt pool. These Marangoni flows can change direction during solidification depending on the transition temperature of the surface tension temperature dependence, and are highly sensitive to the sulfur content of the alloy, even in the ppm range. A higher sulfur content will increase this transition temperature, enabling radially inward fluid flows earlier in the solidification process. Surface tension measurements are generally difficult to perform, so available values for Inconel 718 with varying sulfur contents consistent with the chemical composition of the sample were taken from Lee et al. [36].

3 Results

3.1 3D Microstructure

The fully reconstructed volume is shown in Figure 2(a). The bulk microstructure of the sample is strongly textured, with large columnar grains that are well-aligned with the build direction of the block. These columnar grains with <001>-type orientations form via epitaxial growth from subsurface layers, which are remelted multiple times as additional layers of material are deposited. The top surface of the block shows periodic surface roughness that forms line artifacts on the surface of the build, which arise from the bidirectional raster scan strategy used to fabricate the blocks. After reaching steady state build conditions, the single spot melt was deposited onto a fresh layer of powder, resulting in the roughly circular melt pool that interrupts the linear artifacts seen across the rest of the top surface.

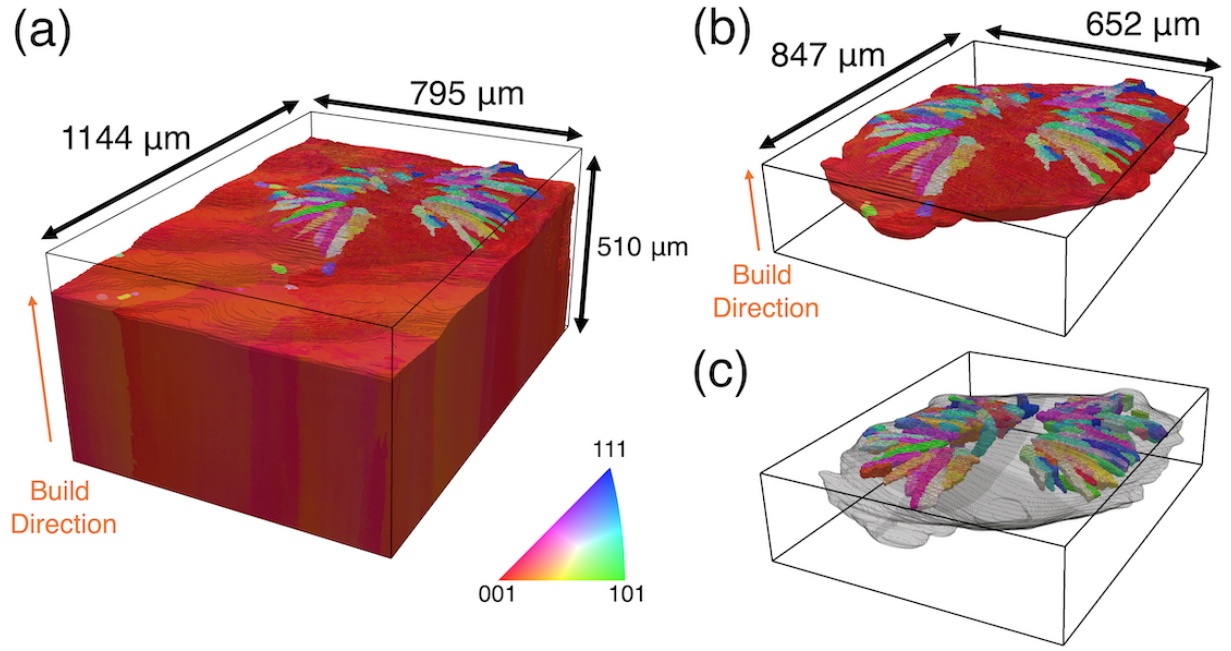

Fig. 2 3D EBSD data of Inconel 718 from TriBeam tomography. Fully reconstructed volume of isolated melt pool and surrounding bulk material on top surface of EBM build (a). Melt pool volume segmented from the bulk using BSE images (b). Nucleated grains that are fully contained within the melt pool volume form radially around the center of the melt pool near the top surface(c). All EBSD is shown in inverse pole figure (IPF) coloring, with the build direction taken as the reference direction.

The isolated melt pool was segmented from the bulk using BSE images collected during serial sectioning, which provide strong contrast at the melt pool boundary, as shown in Figure 1. Below the isolated melt pool, arrays of dendrites from the bulk grains are visible in images of the laser machined surface, but these features are not visible within the melt pool, most likely due to the differing thermal gradients generated by the spot melt. The use of the TPS algorithm to align the BSE and EBSD references frames enables segmentation of the melt pool volume from the EBSD data, which is shown in Figure 2(b).

The melt pool has a roughly circular boundary on the build surface, with a small depression in the center, indicative of shrinkage occurring at the end of solidification as the melt pool contracts. Although a large portion of the melt pool contains resolidified portions of the bulk grains, nucleated grains with differing orientations are spread radially around the center of the melt pool. As the isolated spot melt will solidify radially from the melt pool boundary inwards, the maximum thermal gradient direction will point toward the center of the melt pool. Any grains that were partially remelted, including the large bulk columnar grains and any stray nucleated grains, will resolidify along their <001>-type directions toward the center of the melt pool, as this is the standard growth direction for cubic materials [37]. The changing thermal gradient direction is evident in the two grains depicted in Figure 3. Both a large bulk grain, with crystallographic orientation near [001] with respect to the build direction (red IPF coloring) and a stray nucleated grain, with orientation near [111] with respect to the build direction (blue IPF coloring) lie across the melt pool boundary. These two grains maintain their base crystallographic orientation but grow perpendicularly along their respective <001>-type directions toward the center of the spot melt.

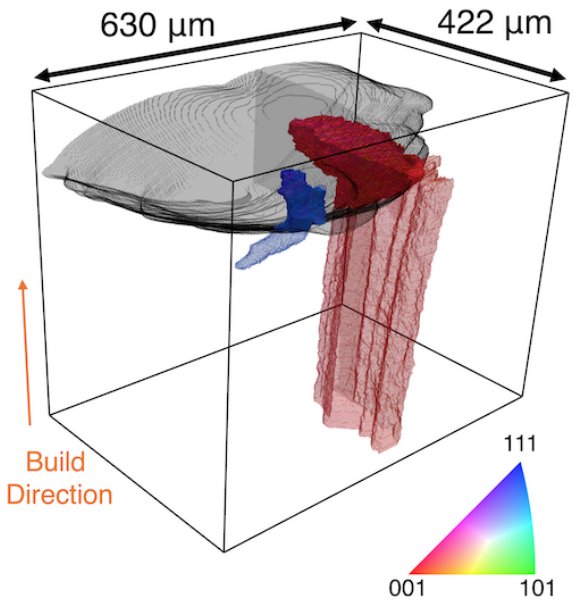

Fig. 3 Remelted grains lying across the spot melt pool boundary. The changing thermal gradient direction imposed by the spot melt results in perpindicular growth of these two grains from their initial growth direction. The portion of the grains lying outside the spot melt pool are semi transparent, while the portion of the grains within the melt pool are opaque. The melt pool boundary is shown as a semi-transparent gray surface. IPF coloring is shown using the build direction as the reference direction.

Segmentation of the spot melt pool boundary enables a direct measurement of the fraction of nucleated grains that form during the single solidification event. Only grains fully contained within the melt pool

boundary were considered for determination of a nucleated grain fraction, as any grains crossing the melt pool boundary were formed prior to the formation of the spot melt. The nucleated grains contained within the melt pool are shown in Figure 2(c), and account for 11.4% of the melt pool volume. These approximately columnar grains have no discernible texture with respect to the build direction as shown by their inverse pole figure (IPF) coloring. The nucleated grains also lie only on the top surface of the melt pool, and are not found in the center of melt pool, which is comprised of epitaxially-grown columnar grains.

3.2 Simulations

Calculated thermal gradients (G) and solid-liquid interface velocities (R) during solidification from three TRUCHAS simulations are shown in Figure 4. The three simulations show qualitatively similar behavior, with lower interface velocities and higher thermal gradients at the beginning of solidification (lower right portion of Figure 4), and higher interface velocities and lower thermal gradients at the end of solidification (upper left portion of Figure 4). All three simulations generally fall within the same range of G and R, with calculated gradients in the range of 10^4 to 10^6 K/m and interface velocities in the range of 10^{-3} to 1 m/s. Although incorporation of the fluid flow in the simulation does not affect the overall trend of G and R during solidification, there are differences at both the early and late stages of solidification. Generally, incorporation of fluid flow decreases the initial interface velocity at the beginning of solidification and increases the final interface velocity at the end of solidification. This effect is greater in the simulation that incorporates fluid flow for a high sulfur content.

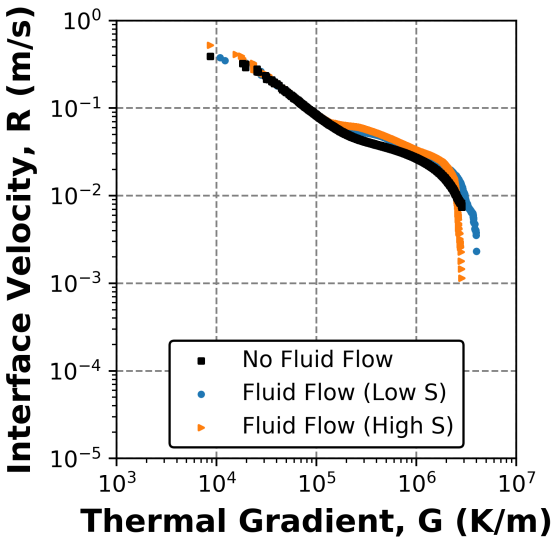

Fig. 4 Calculated thermal gradients (G) and solid-liquid interface velocities (R) from TRUCHAS simulations. The three simulated cases show qualitatively similar behavior throughout solidification, but the incorporation of fluid flow in the simulation creates a wider range of interface velocities. Solidification begins at the edges of the melt pool in the lower right portion of the figure. As solidification proceeds, G will decrease and R will increase, resulting in late stages of solidification at the upper left portion of the figure.

The differing G and R at early and late stages of solidification manifest in an altered melt pool shape and local solidification time, as shown in Figure 5. Local solidification time is measured as the time a volume element (voxel) in the simulation spends between the equilibrium liquidus and solidus temperatures, equivalent to the time the voxel spends in the mushy zone. 3D renderings of the melt pool volumes demonstrate the impact of fluid flow on the melt pool shape. The simulation that only incorporates heat transfer is fully radially symmetric, whereas the low sulfur simulation is shallower and wider, particularly at the top of the melt pool, which spreads out significantly at the edges. The high sulfur simulation is narrower and deeper than the low sulfur case, with a higher average local solidification time. The heat transfer simulation has the narrowest range of local solidification time. Although incorporation of fluid flow does not significantly change the average solidification time, the range of solidification times was nearly doubled as compared to the simulation without fluid flow.

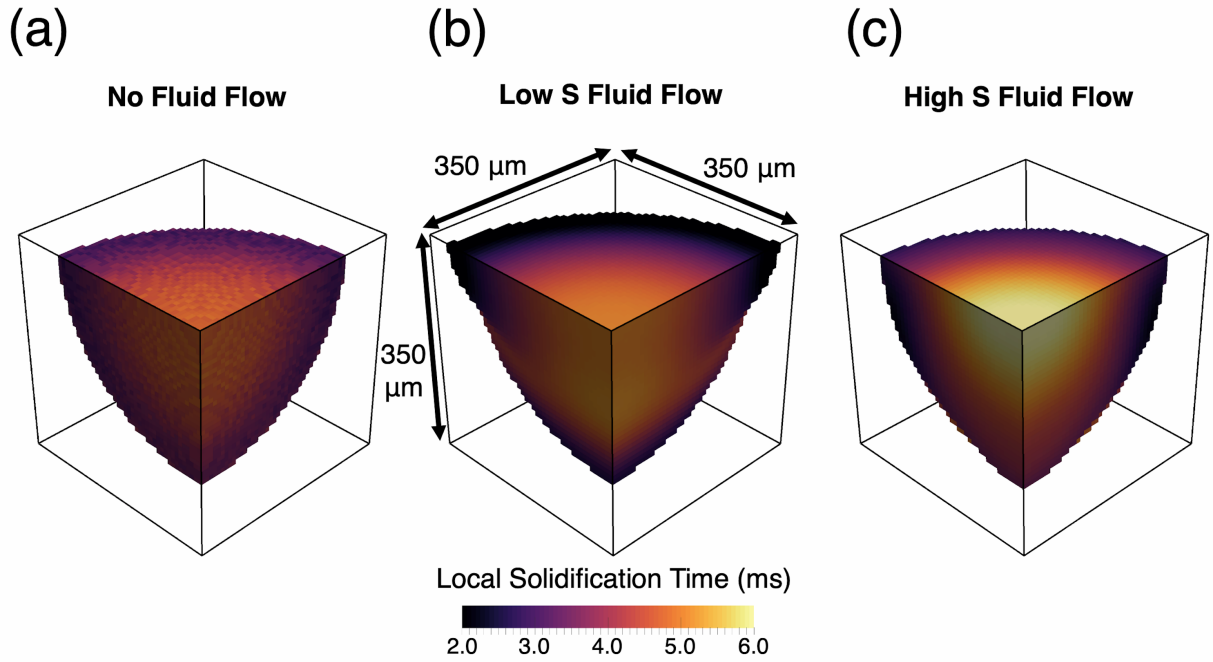

Fig. 5 Melt pool shape and local solidification time. 3D volume representations of the solidified portions of the melt pool for the simulation with heat transfer only (a), fluid flow with low sulfur content (b) and fluid flow with high sulfur content (c). The heat transfer simulation is fully symmetric, whereas the fluid flow simulations decrease local solidification time at the pool edges and increase local solidification time at the pool center.

To better understand the impact of fluid flow, several snapshots of the simulations are shown in Figure 6. These are a series of cross-sections showing the temperature profile and direction of fluid flow within the melt pool. Fluid flow velocities are displayed as arrows, whose direction and size indicate the direction and magnitude of flow within the mushy zone for a given time step. Without fluid flow, the arrows are fully symmetric and point along the maximum thermal gradient direction toward the pool center. With fluid flow, however, the temperature-dependence of surface tension in the molten alloy creates gradients in surface tension which establish fluid vortices within the melt pool. In the low sulfur simulation, a radially outward fluid flow is established in the early stages of solidification by 4 ms due to the negative dependence of surface tension with temperature in the super-heated liquid. As solidification progresses, radially inward flow dominates because the liquid temperature drops and surface tension begins to decrease with decreasing

temperature. This transition from radially outward to radially inward flow will occur at a higher temperature in the high sulfur simulation, which provides additional time for radially inward flows to develop. The lower surface tension at a given temperature for the high sulfur case also enables higher magnitude flows to establish, which are shown by the larger magnitude arrows in this simulation. The last snapshot at 10 ms also demonstrates differences in total solidification time for the various simulations, with the heat transfer simulation having the largest remaining melt pool volume and the high sulfur simulation having the least.

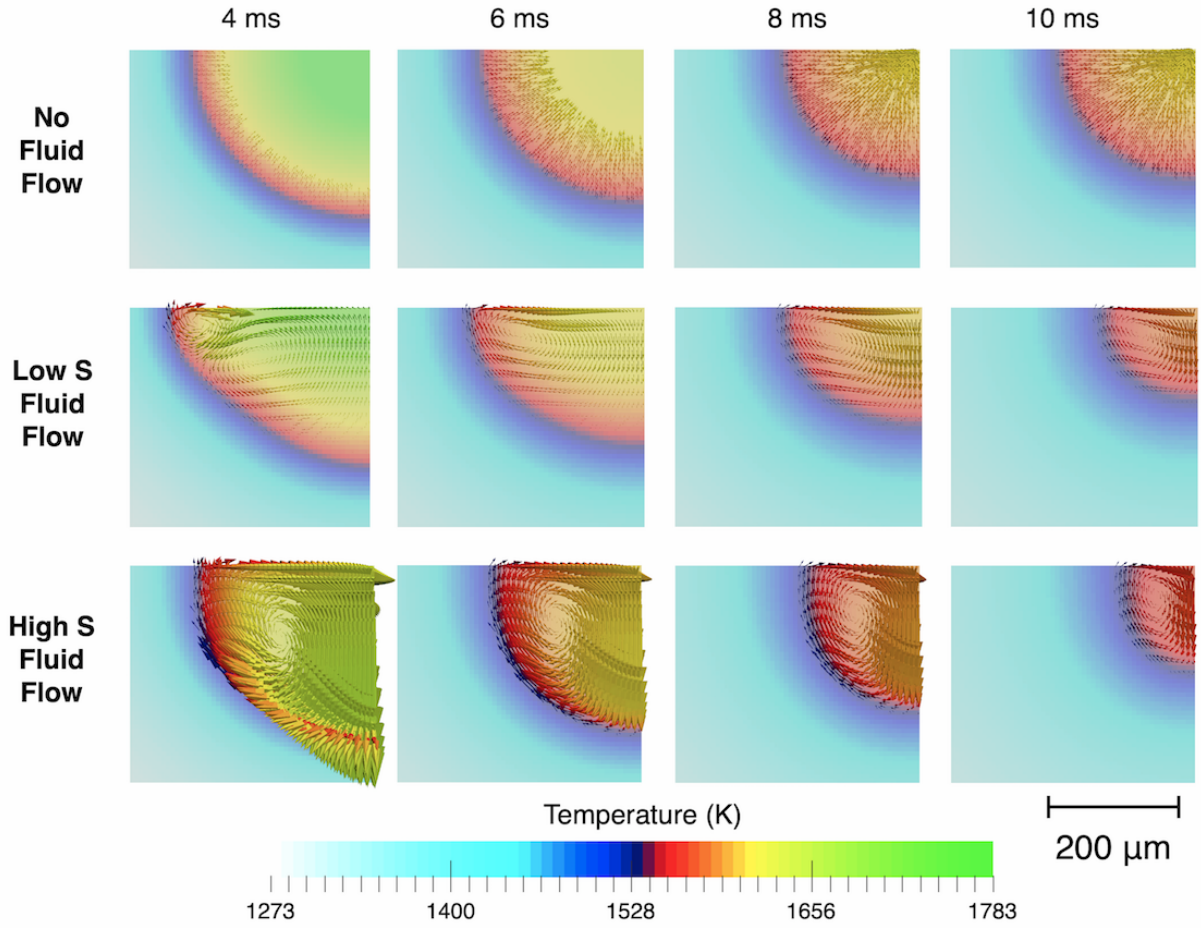

Fig. 6 2D snapshots from different time steps of TRUCHAS simulations performed for Inconel 718. Fluid flow directions are shown using arrows with size directly proportional to the magnitude of the velocity. When fluid flow is incorporated into the simulations, radially inward flow dominates for the most of the solidification event. Material below the solidus temperature is depicted in colors ranging from white (preheat temperature) to blue (solidus temperature), the mushy zone is depicted in colors ranging from red to green (liquidus temperature), and material above the liquidus temperature is shown in solid green.

3.3 Calibrated Microstructure Prediction Model

As TRUCHAS does not incorporate microstructure prediction directly, an additional model is required to predict microstructure given simulated thermal data. Solidification will begin epitaxially from the base metal with a columnar morphology. Depending on thermal conditions experienced as solidification progresses, grains may nucleate in front of the advancing interface to initiate the CET. Here we use a model derived from Hunt's

criterion [19], which describes the CET as occurring when nucleated grains begin to block the advancing columnar front. The transition to fully equiaxed growth is achieved when the columnar front is completely blocked by nucleated grains. Hunt's criterion can be expressed in its general form via the following equation:

$$G = \frac{1}{n+1}\sqrt[3]{\frac{-4\pi N_0}{3\ln[1-\phi]}} \cdot \left(1 - \frac{\Delta T_n{}^{n+1}}{(a \cdot R)^{(n+1)/n}}\right) \cdot (a \cdot R)^{1/n} \tag{3}$$

Where G is the thermal gradient, N_0 is the nuclei density, ϕ is the equiaxed grain fraction, ΔT_n is the critical undercooling to activate nuclei, R is the solid-liquid interface velocity, and parameters a and n are alloy-dependent material parameters. Gäumann et al. [20,38] modified Hunt's criterion to the high thermal gradients present in typical welding processes, which simplifies the relationship by removing the dependence on nuclei activation, given by:

$$G = \frac{1}{n+1}\sqrt[3]{\frac{-4\pi N_0}{3\ln[1-\phi]}} \cdot (a \cdot R)^{1/n} \tag{4}$$

Gäumann et al. investigated autogenous laser welds on CMSX-4 for the epitaxial-laser metal forming (E-LMF) process, which is similar to the directed energy deposition (DED) techniques utilizing blown powder in modern AM processes. A key parameter of this model is the nuclei density, N_0, which is generally not possible to directly measure given a single 2D cross-section. Gäumann et al. were able to estimate N_0 in CMSX-4 by correlating the measured number of nucleated grains in several cross-sections of steady-state autogenous welds as a function of $\frac{G^n}{R}$ for various welding conditions, ultimately determining a nuclei density of 2.0×10^{15} m^{-3} [20]. However, given the full 3D characterization performed on the isolated melt pool in Inconel 718, a direct measurement of nucleated grain density is possible. A total of 259 grains exist within the 3D volume, 206 of which can be said to nucleate in the melt pool as they are fully contained within its boundaries (Figure 2(c)). Using the melt pool volume of 38.4 nL, we have a measured value of 5.4×10^{12} m^{-3} nucleated grains. Just as with the measurements taken from multiple cross-sections, this represents a lower bound of nuclei density that could be resolved with the given imaging technique of EBSD in both cases.

The material constants a and n are dependent on the undercooling at the dendrite tip, which fits the following form:

$$\Delta T_{tip} = (a \cdot R)^{1/n} \tag{5}$$

This form of the relationship is generally true for most solidification conditions, the major exception being near planar front growth conditions at low growth velocity, similar to those used for single-crystal casting [19]. These constants are alloy-specific and only applicable over a limited range of solidification velocities, so it is necessary to calculate the undercooling at the dendrite tip over a wide range of velocities in order to ensure an optimal fit. Despite significant differences in solidification behavior and alloy composition between CMSX-4 and commonly-studied nickel-superalloys for additive manufacturing, alloy constants for CMSX-4 are typically used when applying Gäumann's model. To determine these material parameters more accurately for Inconel 718, we follow the approach of Gäumann et al. using the Ivantsov-Marginal Stability (IMS) model developed by Langer for a paraboloidal dendrite tip growing at marginal stability [38–40].

Relevant material constants, including liquidus slopes and partition coefficients for Inconel 718 were taken from a Scheil analysis performed by Boettinger [41], who helped develop the routines for multi-component Scheil analysis with the CALPHAD approach [42]. The results of the undercooling calculation over the

relevant velocity range are shown as a function of velocity in Figure 7, which also includes the original data for CMSX-4 as calculated by Gäumann for the E-LMF process [43]. There are key differences between these two alloys and processes that this analysis highlights, namely there are a wider range of relevant solidification velocities for the EBM process as compared to the E-LMF process, and in general the material constants calculated for CMSX-4 do not accurately capture the undercooling at the dendrite tip in Inconel 718, particularly at higher interface velocities. Inconel 718 shows less undercooling for all interface velocities, indicating it is a less strongly segregating alloy than CMSX-4. Fits for material constants for E-LMF of CMSX-4 were $a = 1.25 \times 10^6 (\frac{K^n}{m \cdot s})$ and $n = 3.4$ over the relevant velocity regime. Fits for material constants for EBM of Inconel 718 are $a = 1.23 \times 10^5 (\frac{K^n}{m \cdot s})$ and $n = 3.13$.

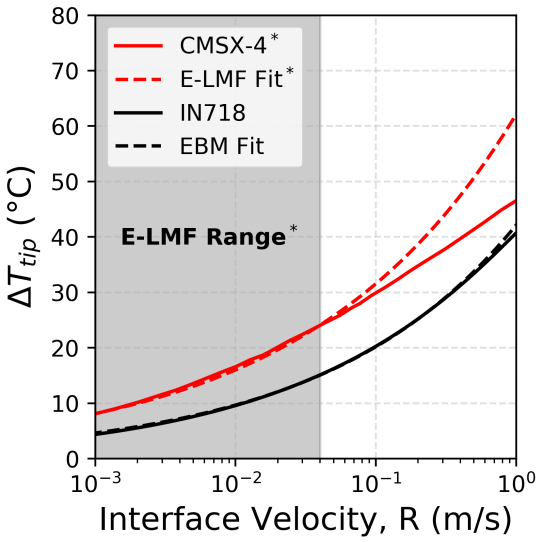

Fig. 7 Dendrite tip undercooling as a function of interface velocity calculated via the IMS model for CMSX-4 and Inconel 718. Data for CMSX-4 and fits for the E-LMF process from [43].

.

Given G and R at every voxel in the TRUCHAS simulations, Equation 4 can be rearranged to solve for ϕ, which represents the likelihood to nucleate grains at that point. The total expected nucleated grain fraction for the entire melt pool, Φ, can then be determined as the volume weighted average from the simulation following Raghavan et al. [18]:

$$\Phi = \frac{\sum V_i \phi_i}{\sum V_i} \tag{6}$$

Where V_i is the volume of the voxel in the simulation. The predicted nucleated grain fractions for each of the three simulations are shown in Table 2 for different combinations of the nuclei density and material constants developed by Gäumann et al. for E-LMF of CMSX-4 and those determined in this work for EBM of Inconel 718. Constants from Gäumann et al. do not give good agreement with the experimentally observed nucleated grain fraction of 11.4%. Use of the fully calibrated model, however, using the directly determined nuclei density and calculated material constants for Inconel 718, achieves the best agreement with experimental observations in the high sulfur fluid flow simulation, with a difference in nucleated grain

Table 2 Results of Microstructure Prediction Model

			Predicted Nucleated Grain Fraction (Φ)		
Nuclei Density (m^{-3})	**a ($\frac{K^n}{m \cdot s}$)**	**n**	*Heat Transfer Only*	*Fluid Flow Low S*	*Fluid Flow High S*
2.0×10^{15}	1.25×10^{6}	3.4	61.6 %	71.8 %	81.8 %
2.0×10^{15}	1.23×10^{5}	3.13	45.8 %	57.4 %	70.9 %
5.4×10^{12}	1.25×10^{6}	3.4	5.6 %	10.4 %	19.9 %
5.4×10^{12}	1.23×10^{5}	3.13	2.6 %	5.1 %	10.8 %

Values from Gäumann et al. [20]
Values from this work

fraction of only 0.6%. The sulfur content used for surface tension values in this simulation was 20 ppm, which is very close to the measured sulfur content of 18 ppm from the AM build.

4 Discussion

Additive processing of the block up to a height of 15 mm ensures the EBM process has reached steady-state build conditions, ensuring the isolated spot melt is created on an additively manufactured substrate under additive processing conditions. This can be a major drawback in single-track melting experiments, which may use conventionally wrought or cast substrates for welding studies but critically fail to capture the effects of powder agglomeration and the complex thermal histories present in AM processing. Powder-powder interactions and wetting effects due to surface roughness, for example, are not easily captured without the use of AM substrates.

Full 3D characterization of the melt pool enables a more thorough analysis of the solidification process than can be achieved through conventional 2D metallography. This analysis relied on multi-modal data to both identify nucleated grains and to isolate the melt pool boundary. The use of multi-modal data collection, both in 2D and 3D, requires robust registration algorithms to fully leverage advanced characterization techniques. The thin plate spline algorithm described in Section 2.1.3 was useful in achieving this registration, but requires significant user input and tuning to acquire a good fit. Progress in machine learning and forward modeling approaches could create more robust, more automated algorithms that take into account the geometry of the detectors within the microscope as well as the source of the signal (secondary electrons, backscattered electrons, etc.) to achieve distortion-free registration of large data volumes.

The vast parameter space offered by AM machines precludes exhaustive experimental studies to determine empirical relationships. The adoption of AM components in critical applications necessitates the use of thermal modeling tools as a key element of the so-called "digital twin" framework to predict part properties without the need for destructive characterization [44]. However, a significant gap still remains in computationally affordable models that can capture all of the relevant physics occurring in the melt pool over length scales relevant to entire AM parts. The close agreement of G and R in all three TRUCHAS simulations shown in Figure 4 suggests that simplified models that only consider heat transfer should qualitatively capture the thermal history behavior, creating a potential pathway for simulation of full-scale parts. However, small changes in the simulated thermal history data, particularly at the beginning and end of solidification, can create large changes in the predicted nucleated grain fraction.

The presence of impurities in AM powder is an important consideration in controlling material properties, both for surface-active elements like sulfur and oxygen that can affect melt pool shape [45], and how impurities may lead to the formation of deleterious precipitates such as nitrides, which can serve as nucleation sites for fatigue cracks in Inconel 718 [46]. Figure 6 shows that strong radially inward fluid flows are established early in the solidification process, which can explain the radial distribution of nucleated grains. The <001>-type growth directions of the nucleated grains, well-aligned with the major axis of the grain, indicate solidification growth toward the center of the melt pool. Any activated solidification nuclei in front of the advancing solid-liquid interface are brought up from the bottom to the top of the melt pool. The growing nuclei are caught in the advancing interface and begin to grow toward the pool center, which has been observed previously in the trapping of alumina particles in larger spot melts of Inconel 718 [36, 47]. The coupling of advanced characterization with modeling provides a more complete understanding of microstructure evolution during additive manufacturing.

Table 2 shows the sensitivity of the microstructure model to both different constants and simulation data. The original formulation of the model over predicts the nucleated grain fraction due to critical differences in material properties and processing conditions. The microstructure prediction model is most accurate when material- and processing-specific parameters are included with fluid flow. Significant differences in alloy constants between CMSX-4 and Inconel 718 highlight the importance of accurately capturing chemical composition when attempting to predict microstructure. The faster solidification velocities predicted in the EBM process also demonstrate the need to recalculate the material constants for the relevant processing regime. This framework can be easily extended to other well-studied alloy systems through the use of multi-component phase diagrams.

The nuclei density, which is typically used as a calibration value for models, has a more significant impact on the model's prediction. The much lower measured nuclei density observed in the AM sample serves to suppress the CET by minimizing the available sites for grain nucleation. Previous studies in AM have taken advantage of the microstructural sensitivity to nuclei density by incorporating inoculants on the prealloyed powder [48], but these approaches may not be applicable to all alloy systems and processing conditions. The large discrepancy between experimentally determined nuclei in this work and that of Gäumann et al. may not stem simply from material properties; the role of heat sources (laser versus electron beam) in controlling super-heating and energy density in the melt, as well as differences in substrate material (single crystal castings versus AM block) are likely important factors. As only one melt pool was characterized in this work, it is not possible to clearly approximate variability from spot to spot in nucleation density measurements, which is inherently a stochastic process. Nucleation kinetics may also be different in laser powder-bed processes, in which gas flow and vaporization of the metal can create denuded zones as those powder beds are not typically sintered. However, the uniformity of the microstructure in the rest of the build indicates that similar behavior would be expected regardless of the location of the isolated melt pool.

The use of 3D characterization enables a full calibration of the microstructure prediction model that can not only be used to analyze simulation data, but can also be used to generate an updated processing-microstructure map for this AM process. Using Equation 3 and Hunt's original criterion for qualifying growth modes, the CET can be calculated for the full range of G and R for EBM of Inconel 718. Processing maps for the original formulation of the model as well as the updated model for AM processing are shown in Figure 8. The changing material properties and nuclei densities serve to shift the CET to higher interface velocities and lower thermal gradients for the EBM process than for E-LMF. The suppression of the CET

in EBM is likely responsible for the heavily textured, columnar microstructures that are typically observed in AM processes, with any nucleated grains forming near the end of solidification likely being remelted upon subsequent deposition. The processing map calibrated in this work can be extended for microstructure prediction of simulated bulk melting strategies. Continued development of this approach could further enable microstructure prediction of entire parts via simulation.

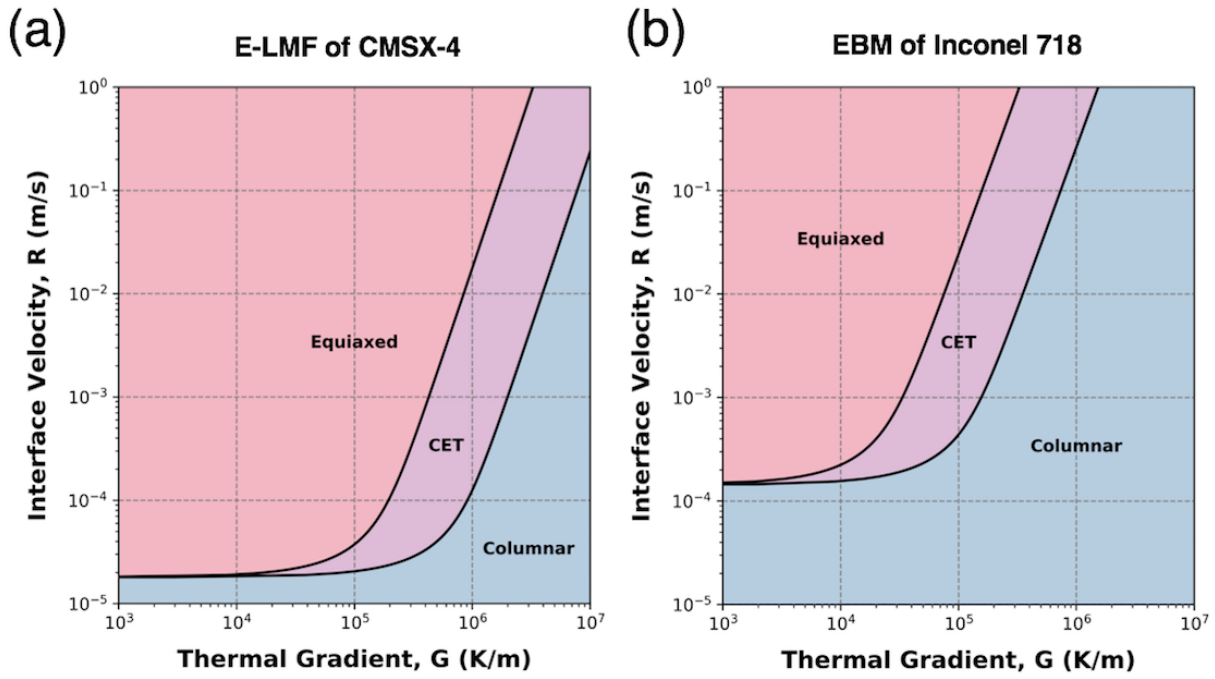

Fig. 8 Microstructure processing maps for epitaxial laser metal forming (E-LMF) of CMSX-4 (a) and electron beam melting (EBM) of Inconel 718 (b). The location of the CET was calculated using Hunt's criterion in Equation 3.

5 Conclusion

A full 3D characterization of an isolated melt pool in AM Inconel 718 has been presented. Experimental characterization and solidification simulations were used to calibrate previous models of the CET developed for a laser-based welding process using a directly measured nuclei density of 5.4×10^{12} m^{-3}. A new microstructure processing map for EBM of Inconel 718 has been developed using this approach, which demonstrates the suppression of the CET in EBM of Inconel 718 as compared to the original model. Advanced characterization techniques are critical for advancing and validating modern modeling approaches, which in turn can help explain the complex microstructures observed in additively manufactured components. This approach also provides a future pathway for achieving location-specific properties through control of scan parameters.

6 Acknowledgements

This research was sponsored by the US Department of Energy, Office of Energy Efficiency and Renewable Energy, Advanced Manufacturing Office, under contract DE-AC05-00OR22725 with UT-Battelle, LLC and performed in partiality at the Oak Ridge National Laboratory's Manufacturing Demonstration Facility, an Office of Energy Efficiency and Renewable Energy user facility. This research was also supported by the Department of Energy RAMP-UP program under award number 4000156470.

7 Conflicts of Interest

On behalf of all authors, the corresponding author states that there is no conflict of interest.

References

1. M. Simonelli, Y.Y. Tse, and C. Tuck. Effect of the build orientation on the mechanical properties and fracture modes of SLM Ti6Al4V. *Materials Science and Engineering: A*, 616:1–11, oct 2014.
2. Wen Shifeng, Li Shuai, Wei Qingsong, Chunze Yan, Zhang Sheng, and Shi Yusheng. Effect of molten pool boundaries on the mechanical properties of selective laser melting parts. *Journal of Materials Processing Technology*, 214(11):2660–2667, nov 2014.
3. Pavel Hanzl, Miroslav Zetek, Tomáš Bakša, and Tomáš Kroupa. The Influence of Processing Parameters on the Mechanical Properties of SLM Parts. *Procedia Engineering*, 100(January):1405–1413, 2015.
4. Luke N. Carter, Christopher Martin, Philip J. Withers, and Moataz M. Attallah. The influence of the laser scan strategy on grain structure and cracking behaviour in SLM powder-bed fabricated nickel superalloy. *Journal of Alloys and Compounds*, 615:338–347, dec 2014.
5. P. Ganesh, R. Kaul, C.P. Paul, Pragya Tiwari, S.K. Rai, R.C. Prasad, and L.M. Kukreja. Fatigue and fracture toughness characteristics of laser rapid manufactured Inconel 625 structures. *Materials Science and Engineering: A*, 527(29-30):7490–7497, nov 2010.
6. A.A. Antonysamy, J. Meyer, and P.B. Prangnell. Effect of build geometry on the β-grain structure and texture in additive manufacture of Ti6Al4V by selective electron beam melting. *Materials Characterization*, 84:153–168, oct 2013.
7. Harald Ernst Helmer, Carolin Körner, and Robert Friedrich Singer. Additive manufacturing of nickel-based superalloy Inconel 718 by selective electron beam melting: Processing window and microstructure. *Journal of Materials Research*, 29(17):1987–1996, sep 2014.
8. Xibing Gong, Ted Anderson, and Kevin Chou. Review on powder-based electron beam additive manufacturing technology. *Manufacturing Review*, 1:2, apr 2014.
9. M. M. Kirka, K. A. Unocic, N. Raghavan, F. Medina, R. R. Dehoff, and S. S. Babu. Microstructure Development in Electron Beam-Melted Inconel 718 and Associated Tensile Properties. *JOM*, 68(3):1012–1020, mar 2016.
10. Carolin Körner, Harald Helmer, Andreas Bauereiß, and Robert F. Singer. Tailoring the grain structure of IN718 during selective electron beam melting. *MATEC Web of Conferences*, 14:08001, aug 2014.
11. Lakshmi L. Parimi, Ravi G. A., Daniel Clark, and Moataz M. Attallah. Microstructural and texture development in direct laser fabricated IN718. *Materials Characterization*, 89:102–111, mar 2014.
12. R. R. Dehoff, M. M. Kirka, F. A. List, K. A. Unocic, and W. J. Sames. Crystallographic texture engineering through novel melt strategies via electron beam melting: Inconel 718. *Materials Science and Technology*, 31(8):939–944, jun 2015.
13. R. R. Dehoff, M. M. Kirka, W. J. Sames, H. Bilheux, A. S. Tremsin, L. E. Lowe, and S. S. Babu. Site specific control of crystallographic grain orientation through electron beam additive manufacturing. *Materials Science and Technology*, 31(8):931–938, jun 2015.
14. Colt Montgomery, Jack Beuth, Luke Sheridan, and Nathan Klingbeil. Process Mapping of Inconel 625 in Laser Powder Bed Additive Manufacturing. *Solid Freeform Fabrication Symposium*, pages 1195–1204, 2015.
15. Saad A. Khairallah, Andrew T. Anderson, Alexander Rubenchik, and Wayne E. King. Laser powder-bed fusion additive manufacturing: Physics of complex melt flow and formation mechanisms of pores, spatter, and denudation zones. *Acta Materialia*, 108:36–45, apr 2016.
16. Manyalibo J. Matthews, Gabe Guss, Saad A. Khairallah, Alexander M. Rubenchik, Philip J. Depond, and Wayne E. King. Denudation of metal powder layers in laser powder bed fusion processes. *Acta Materialia*, 114:33–42, aug 2016.
17. Saad A. Khairallah and Andy Anderson. Mesoscopic simulation model of selective laser melting of stainless steel powder. *Journal of Materials Processing Technology*, 214(11):2627–2636, 2014.
18. Narendran Raghavan, Ryan Dehoff, Sreekanth Pannala, Srdjan Simunovic, Michael Kirka, John Turner, Neil Carlson, and Sudarsanam S. Babu. Numerical modeling of heat-transfer and the influence of process parameters on tailoring the grain morphology of IN718 in electron beam additive manufacturing. *Acta Materialia*, 112:303–314, jun 2016.
19. J. D. Hunt. Steady State Columnar and Equiaxed Growth of Dendrites and Eutectic. *Materials Science and Engineering*, 65:75–83, 1984.
20. M. Gäumann, C. Bezençon, P. Canalis, and W. Kurz. Single-crystal laser deposition of superalloys: processingmicrostructure maps. *Acta Materialia*, 49(6):1051–1062, apr 2001.
21. *Nickel Alloy, Corrosion and Heat Resistant, Bars, Forgings, and Rings 52.5Ni 19Cr 3.0Mo 5.1Cb 0.90Ti 0.50Al 18Fe, Consumable Electrode or Vacuum Induction Melted 1775F (968C) Solution Heat Treated, Precipitation Hardenable*, sep 1965.
22. Andrew T. Polonsky, McLean P. Echlin, William C. Lenthe, Ryan R. Dehoff, Michael M. Kirka, and Tresa M. Pollock. Defects and 3D structural inhomogeneity in electron beam additively manufactured Inconel 718. *Materials Characterization*, 143(January):171–181, sep 2018.

23. McLean P. Echlin, Marcus Straw, Steven Randolph, Jorge Filevich, and Tresa M. Pollock. The TriBeam system: Femtosecond laser ablation in situ SEM. *Materials Characterization*, 100:1–12, feb 2015.
24. McLean P. Echlin, Alessandro Mottura, Christopher J. Torbet, and Tresa M. Pollock. A new TriBeam system for three-dimensional multimodal materials analysis. *Review of Scientific Instruments*, 83(2):023701, feb 2012.
25. C. Harris and M. Stephens. A Combined Corner and Edge Detector. In *Procedings of the Alvey Vision Conference 1988*, pages 23.1–23.6. Alvey Vision Club, 1988.
26. D.G. Lowe. Object recognition from local scale-invariant features. In *Proceedings of the Seventh IEEE International Conference on Computer Vision*, volume 482, pages 1150–1157 vol.2. IEEE, sep 1999.
27. Martin Urschler, Joachim Bauer, Hendrik Ditt, and Horst Bischof. SIFT and Shape Context for Feature-Based Nonlinear Registration of Thoracic CT Images. In R.R. Beichel and M. Sonka, editors, *Lecture Notes in Computer Science*, volume 4241 LNCS, pages 73–84. Springer, Berlin, Heidelberg, 2006.
28. Andrew Deal, David Rowenhorst, Brandon Laflen, Ian Spinelli, Tony Barbuto, Yuchi Huang, and Timothy Hanlon. *Proceedings of the 1st International Conference on 3D Materials Science*. Springer International Publishing, Cham, 2016.
29. Marie-Agathe Charpagne, Florian Strub, and Tresa M. Pollock. Accurate reconstruction of EBSD datasets by a multimodal data approach using an evolutionary algorithm. *Materials Characterization*, 150:184–198, apr 2019.
30. Y.B. Zhang, A. Elbrønd, and F.X. Lin. A method to correct coordinate distortion in EBSD maps. *Materials Characterization*, 96:158–165, oct 2014.
31. F.L. Bookstein. Principal warps: thin-plate splines and the decomposition of deformations. *IEEE Transactions on Pattern Analysis and Machine Intelligence*, 11(6):567–585, jun 1989.
32. Michael A Groeber and Michael A Jackson. DREAM.3D: A Digital Representation Environment for the Analysis of Microstructure in 3D. *Integrating Materials and Manufacturing Innovation*, 3(1):56–72, dec 2014.
33. Stuart I Wright and Matthew M Nowell. EBSD Image Quality Mapping. *Microscopy and Microanalysis*, 12(01):72–84, feb 2006.
34. Andrew T. Polonsky, Christian A. Lang, Kristian G. Kvilekval, Marat I. Latypov, McLean P. Echlin, B. S. Manjunath, and Tresa M. Pollock. Three-dimensional Analysis and Reconstruction of Additively Manufactured Materials in the Cloud-Based BisQue Infrastructure. *Integrating Materials and Manufacturing Innovation*, 8(1):37–51, mar 2019.
35. D. A. Korzekwa. Truchas a multi-physics tool for casting simulation. *International Journal of Cast Metals Research*, 22(1-4):187–191, aug 2009.
36. P. D. Lee, P. N. Quested, and M. McLean. Modelling of Marangoni effects in electron beam melting. *Philosophical Transactions of the Royal Society of London. Series A: Mathematical, Physical and Engineering Sciences*, 356(1739):1027–1043, apr 1998.
37. J.A. Dantzig and M. Rappaz. *Solidifcation*. EPFL Press, first edit edition, 2009.
38. M. Gäumann, R Trivedi, and W. Kurz. Nucleation ahead of the advancing interface in directional solidification. *Materials Science and Engineering: A*, 226-228:763–769, jun 1997.
39. G.P. Ivantsov. Temperature Field Around a Spherical, Cylindrical, and Needle-Shaped Crystal, Growing in a Pre-Cooled Melt. *Doklady Akadmii Nauk SSSR*, 58:567–569, 1947.
40. J.S. Langer and J. Müller-Krumbhaar. Stability effects in dendritic crystal growth. *Journal of Crystal Growth*, 42(C):11–14, dec 1977.
41. William J. Boettinger. The Solidification of Multicomponent Alloys. *Journal of Phase Equilibria and Diffusion*, 37(1):4–18, feb 2016.
42. W.J. Boettinger, U.R. Kattner, S.R. Coriell, Y.A. Chang, and B.A. Mueller. Development of Multicomponent Solidification Micromodels Using a Thermodynamic Phase Diagram Data Base. In *Conference on modeling of casting, welding and advanced solidification processes*, page 1030, London, UK, 1995.
43. Matthias Gäumann. *Epitaxial Laser Metal Forming of a Single Crystal Superalloy*. Docteur és sciences techniques, École Polytechnique Fédérale de Lausanne, 1999.
44. G.L. Knapp, T. Mukherjee, J.S. Zuback, H.L. Wei, T.A. Palmer, A. De, and T. DebRoy. Building blocks for a digital twin of additive manufacturing. *Acta Materialia*, 135:390–399, aug 2017.
45. C R Heiple and J R Roper. Mechanism for Minor Element Effect on GTA Fusion Zone Geometry. *Welding Journal*, 61(4):97s–102s, 1982.
46. Damien Texier, Ana Casanova Gómez, Stéphane Pierret, Jean-Michel Franchet, Tresa M. Pollock, Patrick Villechaise, and Jonathan Cormier. Microstructural Features Controlling the Variability in Low-Cycle Fatigue Properties of Alloy Inconel 718DA at Intermediate Temperature. *Metallurgical and Materials Transactions A*, 47(3):1096–1109, mar 2016.
47. P.N. Quested, D.M. Hayes, and K.C. Mills. Factors affecting raft formation in electron beam buttons. *Materials Science and Engineering: A*, 173(1-2):369–375, dec 1993.
48. John H. Martin, Brennan D. Yahata, Jacob M. Hundley, Justin A. Mayer, Tobias A. Schaedler, and Tresa M. Pollock. 3D printing of high-strength aluminium alloys. *Nature*, 549(7672):365–369, sep 2017.